

# Flexoelectricity-driven softening of bend elasticity leads to spontaneous chiral symmetry breaking in a polar fluid

Aitor Erkoreka,<sup>1</sup> Josu Martinez-Perdiguero,<sup>1</sup> Luka Cmok,<sup>2,3</sup> Ema Hanžel,<sup>2,3</sup> Jordan Hobbs,<sup>4</sup> Calum J. Gibb,<sup>5</sup> Richard J. Mandle,<sup>4,5</sup> Nerea Sebastián,<sup>2</sup> and Alenka Mertelj<sup>2,\*</sup>

<sup>1</sup>*Department of Physics, Faculty of Science and Technology,  
University of the Basque Country EHU, Bilbao, Spain*

<sup>2</sup>*Jožef Stefan Institute, Ljubljana, Slovenia*

<sup>3</sup>*Faculty of Mathematics and Physics, University of Ljubljana, Ljubljana, Slovenia*

<sup>4</sup>*School of Physics and Astronomy, University of Leeds, Leeds, UK*

<sup>5</sup>*School of Chemistry, University of Leeds, Leeds, UK*

(Dated: February 18, 2026)

The origin of recently observed spontaneous chiral symmetry breaking in polar fluids is an unsolved problem, and poses fundamental questions as to how helicoidal structures emerge in systems composed of achiral molecules. We report on the softening of bend elasticity close to such phase transition, showing that flexoelectric coupling between the electric polarization and the bend deformation is the responsible mechanism, presumably arising from the bent shape of the constituent highly polar molecules.

Polarity and chirality are intimately related phenomena in soft matter. In fact, it is the intrinsic chirality of molecules that makes spontaneous polar order possible in the SmC\* phase, the first ever discovered ferroelectric liquid crystalline system [1]. In recent years, the discovery of the ferroelectric nematic (N<sub>F</sub>) phase, a true three-dimensional ferroelectric fluid, has sparked significant interest in the soft matter community [2–6]. In this phase, the longitudinal dipole moments of achiral molecules spontaneously align roughly parallel to each other, thus creating a large electric polarization  $\mathbf{P}$  (where  $|\mathbf{P}| \sim \mu\text{C}/\text{cm}^2$ ), which breaks the inversion symmetry of the director  $\mathbf{n}$ , the unit vector that specifies the average direction of molecular orientation. Although often described as a uniaxial phase, it may adopt a helicoidal structure under certain planar anchoring conditions, owing to a larger reduction in electrostatic energy compared to the associated increase in elastic energy [7]. Following the groundbreaking discovery of the N<sub>F</sub> phase, additional related phases have been identified, making up the so-called ferroelectric nematic realm [8–12]. Particularly noteworthy are those systems exhibiting spontaneous chiral symmetry breaking, like the ferroelectric twist-bend nematic (N<sub>TBF</sub>) and polar helicoidal smectic C (SmC<sub>P</sub><sup>H</sup>) phases [13–15]. Both phases are spontaneously polar and chiral in the bulk, where the helix pitch is on the order of the wavelength of visible light, the difference being that the latter additionally exhibits smectic (one-dimensional quasilong-range positional) order. Interestingly, mixing a compound exhibiting the SmC<sub>P</sub><sup>H</sup> phase (compound **1**) with the prototypical ferroelectric nematogen DIO, the authors found a rich phase diagram, where the phase sequences and transition temperatures can be continuously tuned [14], thus allowing for the comprehensive exploration of the origin and dynamics of the different phases.

In conventional twist-bend nematics (N<sub>TB</sub>) [16], also referred to as polar-twisted nematics (N<sub>PT</sub>) by some au-

thors due to their nanoscale modulation [17, 18], the pre-translational behavior in the N phase is governed by a softening of the bend elastic constant  $K_3$  [19–21]. Different models, both phenomenological and microscopic, have been developed over the years to explain this behavior [22–25]. Ignoring the slight increase of  $K_3$  just before the transition, which is not well understood yet, the overall softening appears to be the result of steric effects related to the bent molecular shape of the mesogens and not due to flexoelectricity [26], as some theories suggested. This is in stark contrast to polar liquid crystals like ferroelectric nematics, where the transition from the high-temperature N phase to the intermediate antiferroelectric splay-modulated N<sub>S</sub> phase [16], characterized by a strong softening of the splay elastic constant  $K_1$ , is driven by the flexoelectric coupling between splay deformation and electric polarization [4, 27]. In this letter, we demonstrate that this same mechanism drives the softening of bend elasticity and the formation of a spontaneously chiral polar mesophase. The studied material is F7 (End Matter, [28]), and Fig. 1 shows the molecular arrangement in the N<sub>F</sub> and N<sub>TBF</sub> phases, as well as their corresponding textures.

Firstly, in order to probe the dipolar fluctuations occurring along the entire phase sequence, we measured the complex dielectric permittivity  $\varepsilon^*(f) = \varepsilon'(f) - i\varepsilon''(f)$  in the frequency range 10 Hz–3 MHz (End Matter). The temperature evolution of the imaginary component of the dielectric spectra can be found in Fig. 2(a). To quantitatively analyze and interpret the dielectric relaxation processes, the spectra at each temperature were fitted to the Havriliak-Negami equation (End Matter). The obtained strengths and frequencies of maximum absorption are shown in Fig. 2(b). The behavior in the N and N<sub>S</sub> phases is similar to that previously found in other ferroelectric nematogens. Usually, these molecules tend to align homeotropically in untreated gold electrodes,

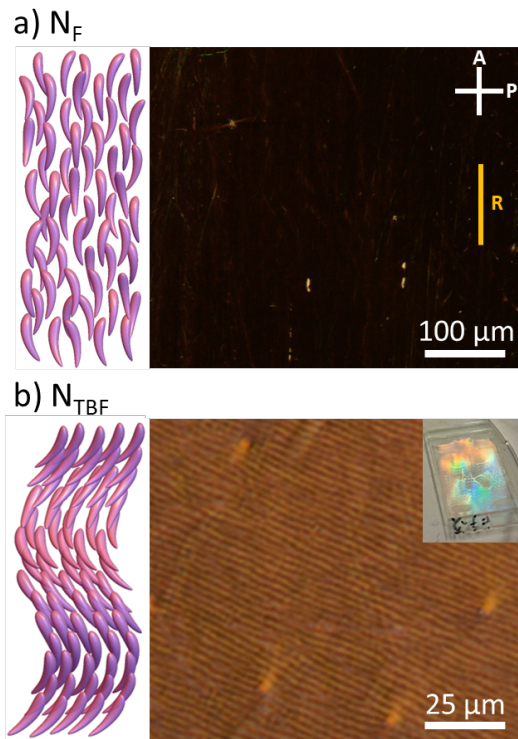


FIG. 1. Schemes and polarized microscope (POM) images of the material F7i in a  $10\ \mu\text{m}$ -thick cell with parallel rubbing. (a)  $N_F$  at  $32^\circ\text{C}$  and (b)  $N_{\text{TBF}}$  just below the  $N_F$ - $N_{\text{TBF}}$  phase transition. P, A, and R denote the polarizer, analyzer, and rubbing directions, respectively. Inset (b) shows a photograph of the cell exhibiting strong Bragg scattering.

as also seems to be the case here judging by the large amplitude of process  $m_1$ . This mode, corresponding to the rotation of individual molecules around their short axis, becomes collective in the  $N_S$  phase and exhibits soft-mode behavior, thereby driving the transition to the lower-temperature  $N_F$  phase. Process  $m_2$ , on the other hand, was observed in the N phase for RM734 in Ref. [4], and more recently for a mixture in Ref. [29]. Its interpretation is currently unclear, although its higher frequency and Arrhenius-type temperature dependence, with an activation energy of  $\sim 74\ \text{kJ/mol}$  (End Matter), suggests it is related to more localized molecular motions. The transition to the  $N_F$  phase is characterized by a strong dielectric response, where a collective relaxation process  $m_{\text{NF,L}}$ , i.e. the Goldstone mode, can be identified at low frequencies. It is well-known that, in order to minimize the depolarization field, the phase transition is accompanied by a change of director orientation from homeotropic to planar [30–32]. There is an additional mode at lower frequencies, which was fitted in order to correctly deconvolute all the contributions to the dielectric spectra, but is ignored in the current discussion since it is likely associated to conductivity effects. As the temperature is lowered, however, another process

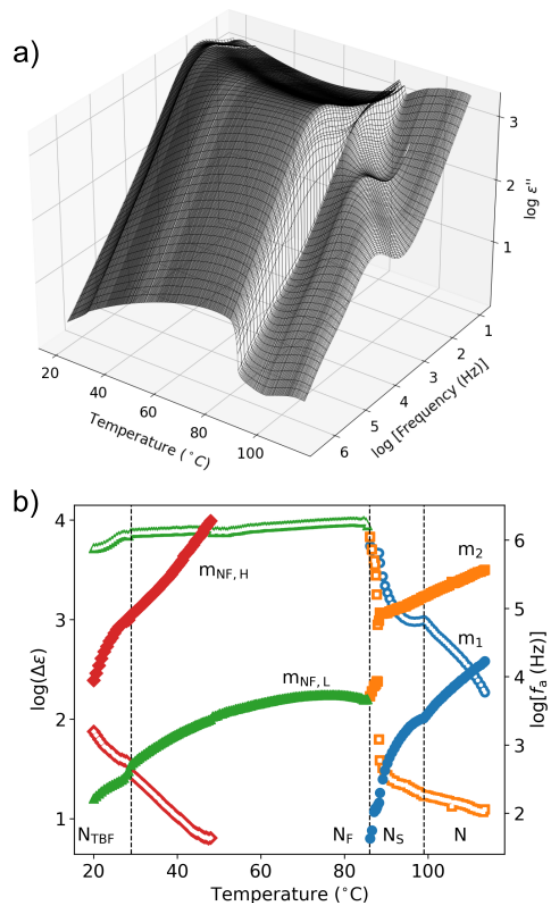


FIG. 2. (a) 3D plot of the dielectric absorption spectra versus temperature. (b) Temperature dependence of the dielectric strengths ( $\Delta\epsilon$ , empty symbols) and frequencies of maximum absorption ( $f_a$ , full symbols) of the different relaxation processes.

$m_{\text{NF,H}}$  enters the available frequency window and can be deconvoluted. Close to the transition to the  $N_{\text{TBF}}$  phase, it slows down considerably and its amplitude increases. We propose that it is related to the rotation of molecules around their long axis, which becomes collective due to the growth of the correlation length of the biaxial order, as will be discussed later.

Interested in the  $N_F$ - $N_{\text{TBF}}$  pretransitional behavior, we set out to study the evolution of orientational fluctuations by dynamic light scattering (DLS) and differential dynamic microscopy (DDM). In the apolar N phase, the orientational fluctuations exhibit two branches: twist-bend and splay-bend. In the  $N_F$  phase, splay deformations are energetically disfavored, leading to suppression of the splay-bend mode. Consequently, in DLS and DDM experiments, the twist-bend branch prevails. The scattering geometries in the DLS experiments were chosen so that only pure bend or pure twist modes with a given scattering vector  $q$  were measured. From the measurements, the temperature dependences of the scat-

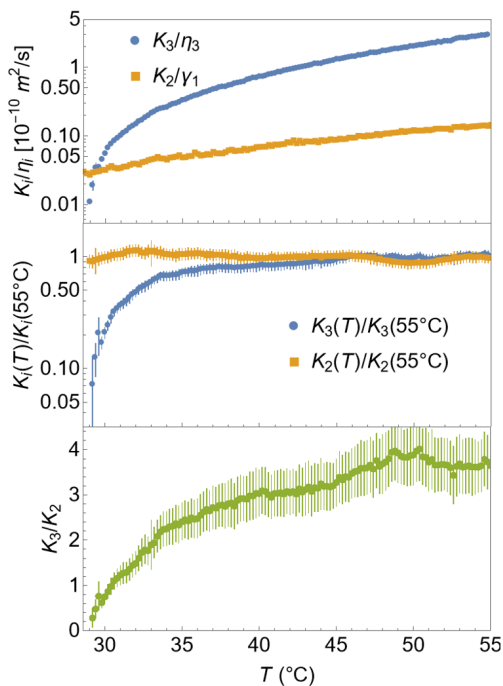


FIG. 3. Temperature dependence of the bend and twist diffusivities (top), normalized bend and twist elastic constants (middle), and ratio  $K_3/K_2$  (bottom).

tered intensity  $I_{T,B} \propto (\Delta\varepsilon_{\text{opt}})^2/(K_i q^2)$ , and relaxation rates  $1/\tau_i = K_i q^2/\eta_i$  were obtained. Here  $i = 2, 3$  denote the twist and bend eigenmodes, respectively,  $K_i$  and  $\eta_i$  are the corresponding elastic constants and viscosities, and  $\Delta\varepsilon_{\text{opt}}$  the anisotropy of the optical dielectric tensor. The twist viscosity  $\eta_2$  equals the rotational viscosity  $\gamma_1$ , while the bend viscosity is smaller due to backflow [33]. Fig. 3 shows the temperature dependence of the bend and twist diffusivities  $K_i/\eta_i$ , elastic constants (the latter normalized at 55°C), and the ratio  $K_3/K_2$ . The latter was determined by combining DDM and DLS results (see End Matter). It is clear that, while  $K_2$  stays practically constant close to the phase transition temperature,  $K_3$  exhibits a pronounced softening.

The simultaneous pretransitional softening of the bend elastic constant and emergent collective dielectric mode is a characteristic of a flexoelectricity-driven phase transition. It is a bend analogous to a ferroelectric-ferroelastic phase transition and can be described in a similar way. Assuming that, in equilibrium, the  $N_F$  phase is uniform and uniaxial, it can be described by the polarization vector  $\mathbf{P} = P_0 \mathbf{n}$ , where  $P_0$  is the polarization amplitude and the director  $\mathbf{n}$  a unit vector. While the splay flexoelectric effect couples  $\mathbf{P}$  to splay deformation, the bend flexoelectric effect couples the polarization perpendicular to  $\mathbf{n}$ , i.e.  $\mathbf{P}_\perp$ , with the bend deformation [34]. Its origin lies in the bent shape of the molecules. In the presence of bend deformation, such bent molecules pack more effi-

ciently when they exhibit orientational order along their long axes [Fig. 4(a)] and, as a consequence, their rotational motion is hindered. Conversely, the presence of orientational order along the long axes promotes bend deformation. As the phase is uniaxial, then  $\langle \mathbf{P}_\perp \rangle = 0$ . Following Longa et al. [24], this polarization does not necessarily correspond to an electric polarization but may instead be related to shape polarity  $\mathbf{b}$ , i.e. a vector order parameter describing the orientational order of the (banana-shaped) molecules around their long axis [Fig. 4(a)]. If such a long-range order exists, the phase is biaxial. Furthermore, if these molecules possess a component of dipole moment perpendicular to their long axes, such an order will also result in a nonzero  $\mathbf{P}_\perp$ . While in an apolar N phase  $\mathbf{P}_\perp$  is parallel to  $\mathbf{b}$ , in the  $N_F$  phase this is no longer the case [Fig. 4(a)]. In general, there is a finite angle between both vectors that depends on the angle between the molecular bend and electric dipole, however, the magnitudes are proportional,  $|\mathbf{P}_\perp| \propto |\mathbf{b}|$ . Here, we are interested in bend fluctuations coupled to fluctuations of  $\mathbf{P}_\perp$ , that is small periodic fluctuations of  $\mathbf{P}_\perp$  and the angle  $\varphi$ , which describes the director  $\mathbf{n} = (\sin(\varphi(\mathbf{q}, t)), \cos(\varphi(\mathbf{q}, t)), 0)$ , with  $\mathbf{q} = (0, q, 0)$  around uniform state with  $\mathbf{P}_\perp = 0$  and  $\mathbf{n} = (0, 1, 0)$ . The relevant part of the free energy density describing these fluctuations is

$$f = \frac{1}{2} K_3 (\mathbf{n} \times (\nabla \times \mathbf{n}))^2 - \gamma_B \mathbf{n} \times (\nabla \times \mathbf{n}) \cdot \mathbf{P}_\perp + \frac{1}{2} a_\perp P_\perp^2 + \frac{1}{2} K_\perp (\nabla P_\perp)^2. \quad (1)$$

The first term is the bend elastic energy density, the second is the flexoelectric term with  $\gamma_B$  being the bend flexoelectric coefficient, and the last two terms are the lowest-order terms in  $\mathbf{P}_\perp$  and its gradients allowed by symmetry. This leads to coupled director and  $\mathbf{P}_\perp$  fluctuation modes with the relaxation rates [35]

$$\frac{1}{\tau_{01}} = \frac{K_3 - \frac{\gamma_B^2}{a_\perp}}{\eta_3} q^2, \quad (2)$$

$$\frac{1}{\tau_{02}} = \frac{a_\perp}{\eta_P} + \left( \frac{K_\perp}{\eta_P} + \frac{\gamma_B^2}{\eta_3 a_\perp} \right) q^2. \quad (3)$$

The first is a hydrodynamic mode and is the one observed in light scattering experiments as a bend mode. The flexoelectric coupling causes the bend elastic constant to be replaced by an effective one  $K_{3,\text{eff}} = K_3 - \gamma_B^2/a_\perp$ . The second mode is dominantly a collective polarization mode measured (at  $q = 0$ ) in dielectric spectroscopy. Analogously to the splay case [4, 35], the amplitude of this dielectric mode is related to  $a_\perp = \frac{1}{\varepsilon_0 \Delta\varepsilon}$  and consequently  $K_{3,\text{eff}} = K_3 - \gamma_B^2 \varepsilon_0 \Delta\varepsilon$ . In normal nematic liquid crystals, the mode associated with the rotation of

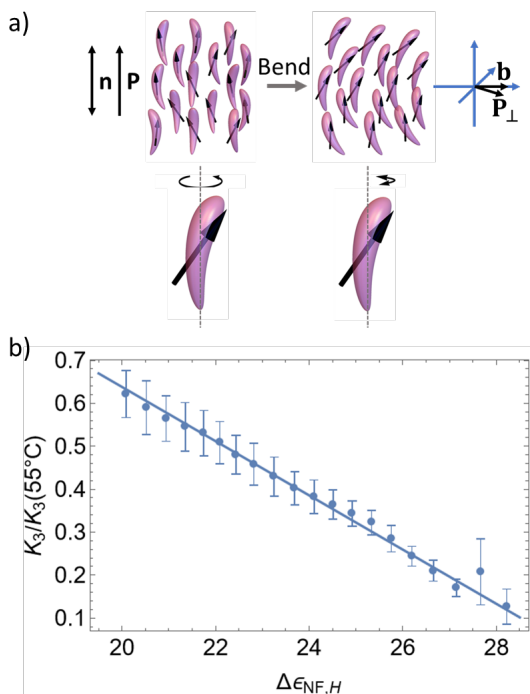


FIG. 4. (a) Dependence of  $K_{3,\text{eff}}/K_{3,\text{eff}}(55^\circ\text{C})$  on the amplitude of the mode  $\Delta\varepsilon_{\text{NF,H}}$ . (b) Schematics of the bend flexoelectric effect in the  $N_{\text{F}}$  phase. Here,  $\mathbf{b}$  is the vector related to shape polarity (see text).

molecules around their long axis is non-collective, fast, and has a small amplitude, so coefficient  $a_{\perp}$  is large and biaxial order is not favorable. However, if such a mode becomes collective, it slows down and its amplitude starts to grow, and causes  $K_{3,\text{eff}}$  to decrease. We propose that the  $m_{\text{NF,H}}$  mode in Fig. 2(b) is causing the softening of the bend elastic constant via bend flexoelectric coupling. Fig. 4(b) shows the dependence of the measured  $K_{3,\text{eff}}/K_{3,\text{eff}}(55^\circ\text{C})$  on the amplitude of the mode  $\Delta\varepsilon_{\text{NF,H}}$  which is linear as predicted by the theory.  $K_{3,\text{eff}}$  approaches zero and the system becomes unstable towards bend deformation. As discussed by Dozov [36], because it is not possible to fill space with homogeneous bend, this leads to the heliconical structure of the  $N_{\text{TBF}}$  phase.

Upon cooling the  $N_{\text{TBF}}$  phase undergoes a transition to  $\text{SmC}_{\text{P}}^{\text{H}}$ . The small angle X-ray scattering (SAXS) shows pretransitional smectic fluctuations already throughout the  $N_{\text{F}}$  phase, which were also previously identified in other ferroelectric nematogens exhibiting the so-called ferroelectric heliconical nematic phase [37]. The amplitude of the peak that corresponds to local smectic order continuously grows with decreasing temperature and exhibits a kink at the  $N_{\text{F}}-N_{\text{TBF}}$  transition (Fig. 5). The  $\text{SmC}$  phase is biaxial, so the  $\text{SmC}$  fluctuations are also fluctuations in biaxial order. These collective fluctuations are detected by BDS because they carry a net dipole moment in the direction perpendicular to the director

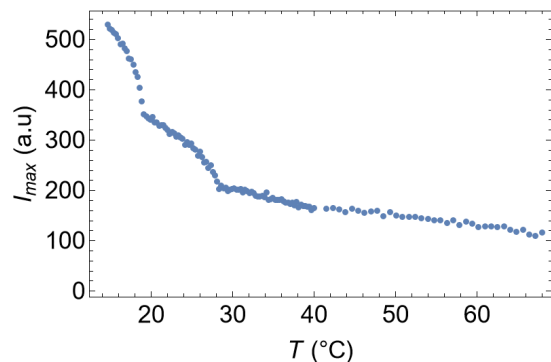


FIG. 5. Temperature dependence of the amplitude of the X-ray scattering peak that corresponds to local smectic order.

and they are coupled to bend through the flexoelectric effect. This explains the continued evolution of this mode in the  $N_{\text{TBF}}$  phase [Fig. 2(b)].

In summary, we have attempted to answer the question regarding the origin of spontaneous chiral symmetry breaking in polar fluids composed of achiral molecules. To this end, we have conducted a series of dielectric, light scattering and X-ray diffraction experiments to examine the pretransitional fluctuations leading to the appearance of a spontaneously chiral polar mesophase. We have simultaneously observed a pretransitional softening of the bend elastic constant and the emergence of a collective dielectric mode, and, through the development of an appropriate theoretical model, we interpret it as a flexoelectricity-driven transition. The data comply with this interpretation and reveal that the bent shape of the constituent highly polar molecules is behind this phenomenon.

A.E. and J.M.-P. acknowledge funding from the Basque Government Project IT1979-26 and from project PID2023-150255NB-I00 from MCIU/AEI/10.13039/5011000-11033/FEDER, UE. J.H., C.J.G. and R.J.M. acknowledge funding from UKRI via a Future Leaders Fellowship, grant No. MR/W006391/1. L.C., E.H., N.S. and A.M. acknowledge the support of the Slovenian Research Agency (Grant Nos. P1-0192, J1-50004, and BI-VB/25-27-011).

\* alenka.mertelj@ijs.si

- [1] R. Meyer, L. Liebert, L. Strzelecki, and P. Keller, *Journal de Physique Lettres* **36**, 69 (1975).
- [2] R. J. Mandle, S. J. Cowling, and J. W. Goodby, *Physical Chemistry Chemical Physics* **19**, 11429 (2017).
- [3] H. Nishikawa, K. Shiroshita, H. Higuchi, Y. Okumura, Y. Haseba, S.-i. Yamamoto, K. Sago, and H. Kikuchi, *Advanced Materials* **29**, 1702354 (2017).
- [4] N. Sebastián, L. Cmok, R. J. Mandle, M. R. de la Fuente, I. Drevenšek Olenik, M. Čopič, and A. Mertelj, *Physical Review Letters* **124**, 037801 (2020).

- [5] X. Chen, E. Korblova, D. Dong, X. Wei, R. Shao, L. Radzihovsky, M. A. Glaser, J. E. MacLennan, D. Bedrov, D. M. Walba, and N. A. Clark, *Proceedings of the National Academy of Sciences* **117**, 14021 (2020).
- [6] N. Sebastián, M. Čopič, and A. Mertelj, *Physical Review E* **106**, 021001 (2022).
- [7] P. Kumari, B. Basnet, M. O. Lavrentovich, and O. D. Lavrentovich, *Science* **383**, 1364–1368 (2024).
- [8] Y. Song, S. Aya, and M. Huang, *Giant* **19**, 100318 (2024).
- [9] H. Kikuchi, H. Matsukizono, K. Iwamatsu, S. Endo, S. Anan, and Y. Okumura, *Advanced Science* **9** (2022), 10.1002/advs.202202048.
- [10] J. Hobbs, C. J. Gibb, and R. J. Mandle, *Small Science* (2024), 10.1002/smsc.202400189.
- [11] J. Hobbs, C. J. Gibb, D. Pocięcha, J. Szydłowska, E. Górecka, and R. J. Mandle, *Angewandte Chemie International Edition* **64** (2024), 10.1002/anie.202416545.
- [12] D. Pocięcha, J. Szydłowska, N. Vaupotič, K. Kwiatkowska, M. Juodka, J. Spiess, J. M. Storey, C. T. Imrie, R. Walker, and E. Gorecka, *Advanced Science* **12** (2025), 10.1002/advs.202508405.
- [13] J. Karcz, J. Herman, N. Rychłowicz, P. Kula, E. Górecka, J. Szydłowska, P. W. Majewski, and D. Pocięcha, *Science* **384**, 1096 (2024).
- [14] C. J. Gibb, J. Hobbs, D. I. Nikolova, T. Raistrick, S. R. Berrow, A. Mertelj, N. Osterman, N. Sebastián, H. F. Gleeson, and R. J. Mandle, *Nature Communications* **15**, 5845 (2024).
- [15] J. Hobbs, C. J. Gibb, and R. J. Mandle, *Nature Communications* **16** (2025), 10.1038/s41467-025-62684-z.
- [16] J. V. Selinger, *Annual Review of Condensed Matter Physics* **13**, 49–71 (2022).
- [17] A. G. Vanakaras and D. J. Photinos, *Soft Matter* **12**, 2208–2220 (2016).
- [18] A. G. Vanakaras, E. T. Samulski, and D. J. Photinos, *Liquids* **4**, 768–781 (2024).
- [19] M. Cestari, S. Diez-Berart, D. A. Dunmur, A. Ferrarini, M. R. de la Fuente, D. J. B. Jackson, D. O. Lopez, G. R. Luckhurst, M. A. Perez-Jubindo, R. M. Richardson, J. Salud, B. A. Timimi, and H. Zimmermann, *Physical Review E* **84** (2011), 10.1103/physreve.84.031704.
- [20] K. Adlem, M. Čopič, G. R. Luckhurst, A. Mertelj, O. Parri, R. M. Richardson, B. D. Snow, B. A. Timimi, R. P. Tuffin, and D. Wilkes, *Physical Review E* **88** (2013), 10.1103/physreve.88.022503.
- [21] V. Borshch, Y.-K. Kim, J. Xiang, M. Gao, A. Jáklí, V. P. Panov, J. K. Vij, C. T. Imrie, M. G. Tamba, G. H. Mehl, and O. D. Lavrentovich, *Nature Communications* **4** (2013), 10.1038/ncomms3635.
- [22] S. M. Shamid, S. Dhakal, and J. V. Selinger, *Physical Review E* **87**, 052503 (2013).
- [23] P. D. Gregorio, E. Frezza, C. Greco, and A. Ferrarini, *Soft Matter* **12**, 5188 (2016).
- [24] L. Longa and G. Pająk, *Physical Review E* **93**, 040701 (2016).
- [25] L. Longa and W. Tomczyk, *The Journal of Physical Chemistry C* **124**, 22761 (2020).
- [26] M. Čopič and A. Mertelj, *Physical Review E* **101**, 022704 (2020).
- [27] P. Medle Rupnik, E. Hanžel, M. Lovšin, N. Osterman, C. J. Gibb, R. J. Mandle, N. Sebastián, and A. Mertelj, *Advanced Science* **12** (2025), 10.1002/advs.202414818.
- [28] A. Sterle *et al.*, (2026), to be submitted.
- [29] E. E. Zavvou, A. Jarosik, H. Nádasi, R. Tuffin, P. K. Karahaliou, C. Krontiras, M. Klases-Memmer, and A. Eremin, *Soft Matter* (2025), 10.1039/d5sm00670h.
- [30] A. Erkoreka, J. Martínez-Perdiguero, R. J. Mandle, A. Mertelj, and N. Sebastián, *Journal of Molecular Liquids* **387**, 122566 (2023).
- [31] A. Erkoreka, A. Mertelj, M. Huang, S. Aya, N. Sebastián, and J. Martínez-Perdiguero, *The Journal of Chemical Physics* **159**, 184502 (2023).
- [32] N. A. Clark, X. Chen, J. E. MacLennan, and M. A. Glaser, *Physical Review Research* **6**, 013195 (2024).
- [33] P.-G. de Gennes and J. Prost, *The physics of liquid crystals*, 2nd ed., International Series of Monographs on Physics (Clarendon Press, Oxford, England, 1995).
- [34] R. B. Meyer, *Physical Review Letters* **22**, 918 (1969).
- [35] N. Sebastián, L. Cmok, A. Petelin, R. J. Mandle, and A. Mertelj, *Liquid Crystals* **51**, 1047 (2024).
- [36] I. Dozov, *Europhysics Letters* **56**, 247 (2001).
- [37] H. Nishikawa, D. Kwaria, A. Nihonyanagi, and F. Araoka, *Advanced Materials* **n/a**, e13451 (2025).
- [38] A. Petelin, 10.5281/zenodo.3800382.

## End Matter

## Materials

In the experiments, a 70:30 mixture of the material DIO and Compound **1**, named F7, from Ref. [14], with phase sequence  $\text{SmC}_P^H$  (20.9°C)  $\text{N}_{\text{TBF}}$  (29.5°C)  $\text{N}_F$  (88.8°C)  $\text{N}_S$  (99.4°C)  $\text{N}$  was used [28]. For the DLS and DDM experiments, 0.06 wt.% of an ionic dye (modified Rhodamine B) was added to the mixture F7, yielding the sample F7i, to achieve stable, uniform in-plane alignment of the director [Fig. 1(a)]. The addition of the dye did not affect the phase transition temperatures. The molecular structures of the employed compounds can be found in Fig. 6.

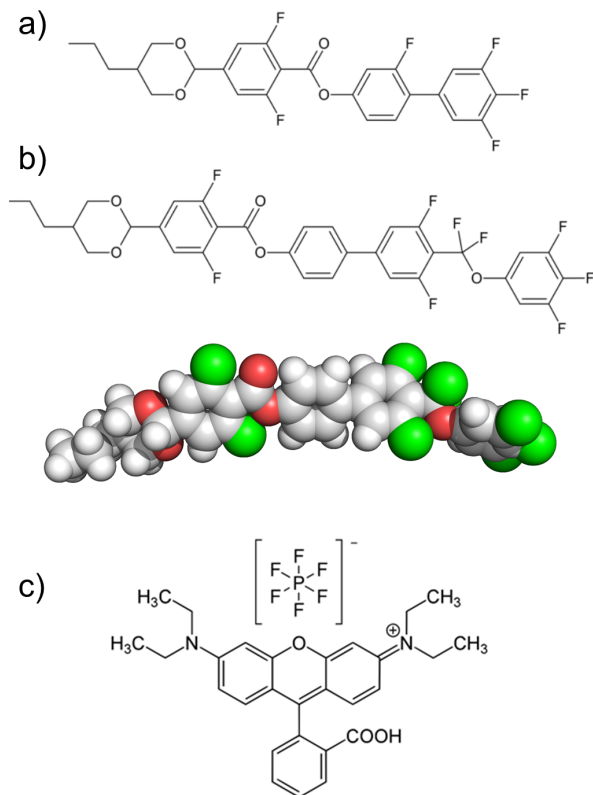


FIG. 6. Molecular structures of (a) DIO, (b) Compound **1** (with its optimized geometry as obtained in Ref. [14] evidencing its slightly bent shape), and (c) Modified RhB.

## BDS

The dynamic dielectric function  $\varepsilon^*(f) = \varepsilon'(f) - i\varepsilon''(f)$  of F7 was measured in the spectral range  $f = 10 \text{ Hz} - 3 \text{ MHz}$  using an Alpha-A impedance analyzer from Novocontrol Technologies GmbH. The sample was placed between two circular gold-coated brass electrodes 5 mm in diameter forming a parallel-plate capacitor, the separa-

tion being fixed at  $d = 20 \mu\text{m}$  by spherical silica spacers. The high conductivity of gold ensured reliable measurements up to the highest frequencies. This cell was then placed at the end of a modified HP 16091A coaxial test fixture, using a Quatro Cryostat for temperature control. No polymer aligning layers were used on the electrodes because, although they can be useful to obtain a proper alignment of liquid crystal molecules, they act as an additional large capacitance in series with the measurement cell and can lead to undesired charge accumulation, among other effects. The oscillator voltage was set to  $0.03 V_{\text{rms}}$  to ensure linear regime. Experiments were done on cooling from  $115^\circ\text{C}$  at  $0.25 \text{ K/min}$ . The stray capacitance of the measurement circuit was subtracted from the measured capacitance, and the complex dielectric permittivity was obtained by dividing this value by the capacitance of the empty cell. Finally, the experimental curves were fitted to Havriliak-Negami (HN) relaxations with a conductivity term:

$$\varepsilon^*(f) = \sum_k \frac{\Delta\varepsilon_k}{\left[1 + \left(\frac{f}{f_k}\right)^{\alpha_k}\right]^{\beta_k}} + \varepsilon_\infty + \frac{\sigma}{\varepsilon_0(i2\pi f)^\lambda}, \quad (4)$$

where  $\Delta\varepsilon_k$ ,  $f_k$ ,  $\alpha_k$  and  $\beta_k$  are respectively the dielectric strength, relaxation frequency and broadness exponents of mode  $k$ ,  $\varepsilon_\infty$  is the high-frequency dielectric permittivity,  $\sigma$  is a measure of the conductivity, and  $0 < \lambda \leq 1$ . Fit examples can be found in Fig. 7.

## DLS

For the DLS experiments, the sample F7i was used to achieve uniform in-plane alignment of the director along the rubbing direction in a liquid crystal cell (EHC, thickness  $10 \mu\text{m}$ , parallel rubbed) in the  $\text{N}_F$  phase. The heating stage (Instec, HCS412W) was used to control the sample temperature. The sample was cooled from  $55^\circ\text{C}$  to room temperature at  $0.02 \text{ K/min}$ . In the DLS setup, a frequency-doubled diode-pumped Nd:YAG laser (532 nm, 80 mW attenuated for 100x), a single mode optical fiber with a GRIN lens connected to an ALV APD based “pseudo” cross-correlation detector, and an ALV-6010/160 correlator was used to obtain the autocorrelation function of the scattered light intensity. The direction and the polarization of the incoming and detected light were chosen so that pure twist and bend modes were observed [35]. The duration of a single measurement was 600 s. The measured intensity autocorrelation function  $g_2$  was fitted by  $g_2 = 2(1 - j_D)j_D g_1 + j_D^2 g_1^2 + y_0$ , where the fitting parameters  $j_D$  and  $y_0$  are the ratio between dynamic and total scattered intensity, and background, respectively, while  $g_1$  was either a single  $g_1 = e^{-t/\tau_T}$

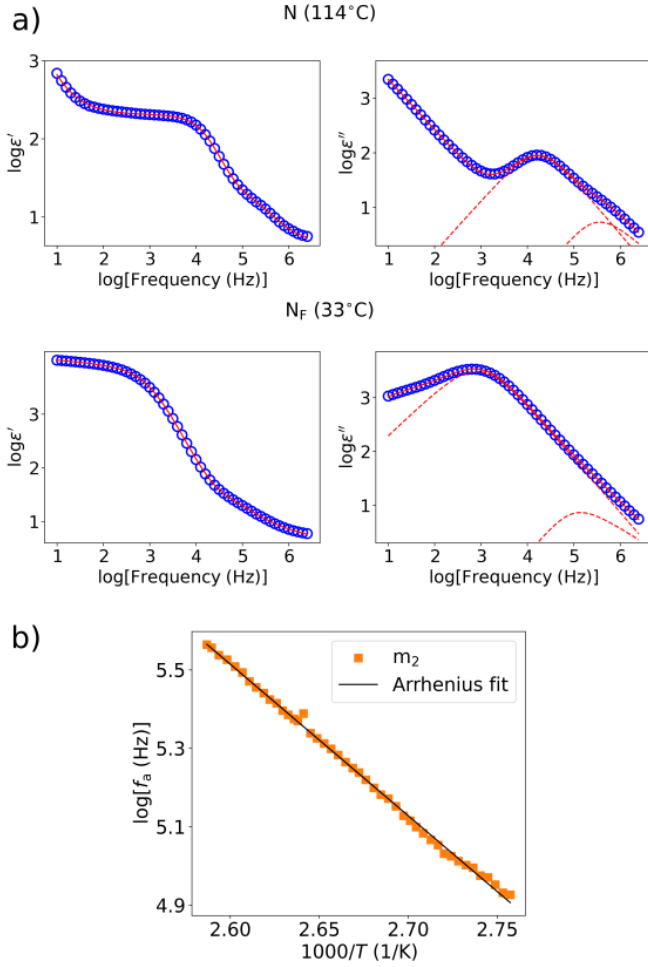


FIG. 7. (a) Examples of Havriliak-Negami fits at representative temperatures. (b) Arrhenius plot for process  $m_2$  giving an activation energy  $E_a \sim 74$  kJ/mol.

(for the twist geometry), or a double exponential function  $g_1 = (1 - a_2)e^{-t/\tau_1} + a_2e^{-t/\tau_B}$  (for the bend geometry). In the bend geometry, besides the dominating bend mode, a weaker and slower mode was observed of which relaxation rate  $1/\tau_1$  did not show significant temperature dependence. In the temperature region below 35°C, it became indistinguishable due to the increasing amplitude and slowing down of the bend mode. From the relaxation rates, the twist  $K_2/\gamma_1$  and bend  $K_3/\eta_3$  diffusivities were calculated. The scattered intensity  $I_{2,3}$  of the twist and bend modes was determined as products  $j_D I_{\text{tot}}$  and  $a_2 j_D I_{\text{tot}}$ , respectively, where  $I_{\text{tot}}$  was the total detected intensity. As in the temperature range between 29°C and 55°C the refractive indices and, consequently, the anisotropy of optical dielectric tensor are almost constant,  $K_{2,3}(T)/K_{2,3}(55^\circ\text{C}) \approx I_{2,3}(55^\circ\text{C})/I_{2,3}(T)$ .

## Differential dynamic microscopy (DDM)

In the DDM experiments, the same sample was used as in the DLS experiments. The heating stage (Instec, HCS302XY) was used to control the sample temperature. The sample was cooled from 35°C to room temperature at 0.02 K/min. Cross DDM setup was used as described in [35]. The angles between the director  $\mathbf{n}$  and the polarizer and analyzer were 80° and 0°, respectively. To calculate the normalized image-cross-correlation function an open-source package `cddm` was used [38]. The correlation functions at all 2D scattering vectors  $\mathbf{q}_{2D} = (q_\perp, q_\parallel)$  with enough signal showed one relaxation which was fitted by a single exponential decay,  $g_{\text{DDM}} = a_0 e^{-t/\tau} + y_0$ . In this geometry, the scattering from twist-bend mode prevails so the 2D dispersion curve  $1/\tau(\mathbf{q}_{2D})$  can be attributed to this mode. Taking into account the relation between the scattering vector  $\mathbf{q}$  and  $\mathbf{q}_{2D}$ ,  $\mathbf{q} = (q_\perp, q_\parallel, q_z)$  with  $q_z \approx q_0 - (q_\perp^2 + q_\parallel^2)/(2k_0 n_e)$ , its relaxation rate as a function of  $\mathbf{q}_{2D}$  can be expressed in terms of 5 parameters:

$$\frac{1}{\tau_{\text{TB}}} = D_0 \times \frac{1 + a_{x2}q_\perp^2 + \frac{a_{x2}^2 q_\perp^4}{4} + a_{y2}q_\parallel^2 + \frac{1}{2}a_{x2}a_{y2}q_\perp^2 q_\parallel^2 + a_{y4}q_\parallel^4}{1 + \frac{a_{x2}q_\perp^2}{2} + b_{y2}q_\parallel^2} \quad (5)$$

The parameters depend on the optic and viscoelastic properties of the material:  $D_0 = K_2 q_0^2 / \gamma_1$ ,  $a_{x2} = (2n_o)/(n_e q_0^2)$ ,  $a_{y2} = (2n_o + n_e(-2 + k_{32} + v_{ca})) / (n_e q_0^2)$ ,  $a_{y4} = (((-1 + k_{32})n_e + n_o)(n_o + n_e(-1 + v_{ca}))) / (n_e^2 q_0^4)$ , and  $b_{y2} = (n_o + n_e(-1 - \alpha_N^2 + v_{ca})) / (n_e q_0^2)$ , with  $n_o$  and  $n_e$  being ordinary and extraordinary index of refraction respectively,  $q_0 \approx (n_e - n_o) \frac{2\pi}{\lambda}$ ,  $k_{32} = \frac{K_3}{K_2}$ ,  $v_{ca} = \frac{\eta_a}{\eta_c}$ ,  $\alpha_N^2 = \frac{\alpha_2^2}{\gamma_1 \eta_a}$ ,  $\eta_{a,c}$  Miesowicz viscosities[33],  $\alpha_2$  Leslie viscosity coefficient [33], and  $\lambda$  wavelength of the LED diode used for the illumination (565nm). All 5 fitting parameters can be reliably obtained from the fitting of  $1/\tau(\mathbf{q}_{2D})$  only in the temperature region of 3K above the phase transition. From the parameters,  $k_{32}$  was extracted and compared to the  $k_{32}(T)/k_{32}(55^\circ\text{C})$  obtained from the DLS measurements [Fig. 3(b)] to determine  $k_{32}(55^\circ\text{C}) = 3.6 \pm 0.3$ .

## SAXS

SAXS patterns of F7 were recorded using a Stoe Stadivari goniometer equipped with a Genix3D microfocuss generator (Xenocs) and a Dectris Pilatus 100K detector. Monochromatic Cu  $K_\alpha$  radiation ( $\lambda = 1.5406$  Å) was employed, setting the exposure time to 1 minute. The temperature was varied using a nitrogen-gas Cryostream controller (Oxford Cryosystems) achieving a temperature

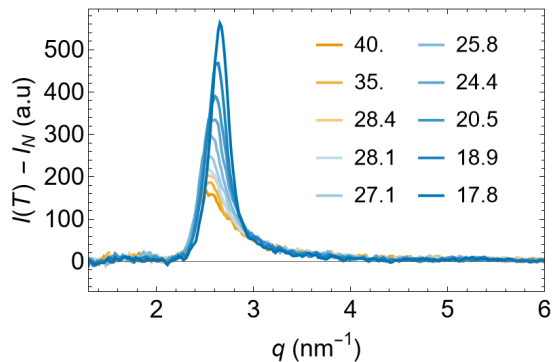


FIG. 8. Temperature evolution of the difference between SAXS intensity  $I(T)$  and SAXS intensity  $I_N$  measured in the N phase at  $110^\circ\text{C}$  showing growing smectic correlations. The labels are the corresponding temperatures in  $^\circ\text{C}$ .

control within  $0.1^\circ\text{C}$ . The material was introduced into a Lindemann capillary 0.6 mm in diameter. Each diffractogram was measured while rotating the capillary by  $360^\circ$  to avoid alignment effects. The peak amplitude shown in Fig. 5 is the peak height extracted from the difference between the SAXS diffractogram  $I(T)$  and the SAXS diffractogram  $I_N$  measured in the N phase at  $110^\circ\text{C}$ ; examples are shown in Fig. 8.